NASA TECHNICAL MEMORANDUM

NASA TM X-68286

NASA TM X-68286

MEASUREMENT OF BEAM DIVERGENCE OF 30-CENTIMETER DISHED GRIDS

by Ronald L. Danilowicz, Vincent K. Rawlin,
Bruce A. Banks, and Edwin G. Wintucky
Lewis Research Center
Cleveland, Ohio 44135

TECHNICAL PAPER proposed for presentation at
Tenth Electric Propulsion Conference sponsored
by the American Institute of Aeronautics and Astronautics
Lake Tahoe, Nevada, October 31-November 2, 1973

MEASUREMENT OF BEAM DIVERGENCE OF 30-CENTIMETER DISHED GRIDS

Ronald L. Danilowicz, Vincent K. Rawlin, Bruce A. Banks,
and Edwin G. Wintucky
National Aeronautics and Space Administration
Lewis Research Center
Cleveland, Ohio

Abstract

The beam divergence of a 30-centimeter diameter thruster with dished grids was calculated from current densities measured with a probe rake containing seventeen planar molybdenum probes. The measured data were analyzed as a function of a number of parameters. The most sensitive parameters were the amount of compensation of the accelerator grid and the ratio of net to total accelerating voltage. The thrust losses were reduced by over 5 percent with the use of compensated grids alone, and by variation of other parameters the overall thrust losses due to beam divergence were reduced to less than 2 percent.

E-7631

Introduction

The electron bombardment ion thruster is being considered for a variety of missions for which the optimum specific impulse is between 2000 and 3000 seconds (refs. 1 and 2). Dished grids (ref. 3) appear attractive for operation in this specific impulse range. Thrust losses due to the use of this type of grid system need, however, to be considered. Ion beam profiles with dished grids are affected by many parameters. This paper presents an experimental investigation of the thrust losses due to ion beam divergence as a function of grid type and geometry over a wide range of thruster operating conditions. Parameters studied included the ratio of net-to-total accelerating voltage, total accelerating voltage, grid hole size, grid percent open area, dish depth, grid spacing, and total ion beam current. In addition, several compensated grid sets for which the center-to-center hole spacing differed for the accelerator and screen grid were tested to determine the effect of hole compensation on beam divergence.

Apparatus and Procedure

Thruster and Facility

The ion beam measurements were all made using a 30-centimeter diameter thruster built by Hughes Research Laboratories (HRL) under Contract NAS3-14140 (ref. 4). The thruster was modified in the course of a separate discharge chamber optimization program. Details of the thruster configurations are presented in a companion conference paper (ref. 5). Twenty-seven different accelerator grid sets were studied during the program. All grid geometry data are presented in table I. These were fabricated by a hydroforming technique similar to that described in reference 3. For some of the grid sets the accelerator grid was stretched prior to hydroforming to compensate for the misalinement normally associated with dished grids. The thruster was operated in the 3.0-meter diameter port of the 7.6-meter diameter by 21.4-meter long vacuum tank at the Lewis Research Center (ref. 6). The bell jar pressure was about 3×10^{-6} torr while the main tank pressure was about 2×10^{-7} torr during thruster operation. All of the data were taken at a constant discharge voltage of 37 volts.

Beam Probe

The measurements were taken with a probe rake consisting of seventeen 1.27-centimeter diameter, planar molybdenum probes. These were equally spaced 15.24 centimeters apart. Each probe was completely shielded on the sides so that current was collected only on the 1.27-centimeter diameter circular face of the probe. This was necessary to define accurately the collecting area. This beam probe rake was swept in an arc in a plane perpendicular to the thruster centerline. This plane was located at both 1.37 or 1.83 meters downstream of the thruster grid system.

The data from the probe rake is automatically recorded using the Central Automatic Digital Data Encoder (CADDE II) system (ref. 7). Data is taken sequentially at a rate of approximately 27 points per second. Potentiometer values are recorded that indicate the position of the probe rake at the beginning and end of each scan of the 17 probes. From these values the position of each probe was determined for the time of its individual reading. Typically, about 45 seconds were required to sweep the rake across the ion beam, and data were taken from each probe approximately 60 times. A total of about 1000 values of current were recorded on magnetic tape.

Computer Code

These data were reduced and analyzed using a digital computer code run on an IBM 7040/7094 direct couple system. The raw data were initially converted into current densities as a function of position. Curve fitting methods (ref. 8) then applied to these values resulted in piecewise continuous functions, continuous in both value and slope, which fit successive intervals of data. These curve fits are used in generating contour plots and also for the integration routines used in analyzing the data.

The integrals necessary to calculate total ion current J_B and the ratio of actual axial thrust to ideal axial thrust T (hereinafter referred to as the thrust factor), were evaluated using a 65 point guass-quadrature numerical integration routine. These quantities were calculated from the following expressions:

$$J_B = \int_0^{2\pi} \int_0^{\infty} j(r,\theta) r \, dr \, d\theta \qquad (1)$$

$$T = \frac{\int_0^{2\pi}\int_0^{\infty} j(r,\theta)\cos\psi \; r \; dr \; d\theta}{\int_0^{2\pi}\int_0^{\infty} j(r,\theta) r \; dr \; d\theta} \qquad (2)$$

where $j(r,\theta)$ is the measured current density at r and θ, cylindrical coordinates in the plane of the probe rake. The coordinate r is measured with respect to the centerline of the thruster and ψ is the angle between the centerline and the line joining the point (r,θ) to the center of the accelerator grid.

Grid Fabrication

All the dished grids discussed in this paper were fabricated by a hydroforming technique, similar to that given in reference 3. Some of the grid sets had larger center-to-center spacing for the accelerator grid to determine the effect on the thrust factor. Several techniques can be used to make the aperature array spacing of the accelerator grid slightly larger (and thus compensating) than that of the screen grid. One technique is to have two different array spaced photoetching master patterns made. Another technique is to use the same array spacing for both the screen and accelerator grid photoetching master pattern but stretch the accelerator grid prior to hydroforming with the screen grid. This latter technique was used for most of the compensated grids discussed in this paper.

The fabrication technique used to stretch the grids to produce a permanent strain consisted of forcing the accelerator grid into a pie pan shape. A stretching system shown in figure 1 was inserted into a hydroforming system shown in figure 2. The grids were either perforated or had a photoresist hole pattern on them prior to stretching. Applying pressure to the water in the upper chamber of the hydroforming system causes the grid to be tightly clamped around its edge. A wedge shaped groove in the clamping ring further prevented irregular slippage of the grid. The application of water pressure to the lower portion of the system caused a disk of metal to be forced into the initially flat accelerator grid. The amount of stretching, ε, was varied by control of the pressure used to raise the metal disk. To prevent scratches on the grids which have photoresist patterns on them the disk had a raised smooth ridge at its edge. After the stretching was accomplished the central flat portion of the grid was cut out, alined with an unstretched screen grid, and as a pair then simultaneously hydroformed using a clamping ring shown in figure 2. The clamping ring allows the grids to hydroform to a natural near-spherical contour. The clamping ring also has a wedge shaped slippage preventing groove machined into it. The groove was found to be important because without it slippage was found to occur causing non-spherical grid contours and local surface flat spots.

Results and Discussion

This section will present the beam divergence and thrust losses associated with a large number of dished grid geometries and thruster operating conditions. Attempts will be made to separate the effect of various parameters on the thrust losses. Because both the screen and accelerator grid are simultaneously hydroformed, the resulting screen and accelerator grids have a geometry shown in figure 3a. For thruster operation the grids are separated by axially displacing one grid downstream of the other, this results in a grid geometry shown in figure 3b. As a result of this geometry there are three thrust losses for each ion beamlet.

The first thrust loss is caused by the misalinement of the screen and accelerator aperatures. This misalinement causes an ion beamlet deflection of an angle λ. All symbols are defined in appendix A and in figure 3b. The second thrust loss is due to the dished grid curvature (associated with the angle γ). Thus, the thrust vector for each beamlet is at an angle of $\lambda + \gamma$ from the thruster axis. Both of these losses are a direct result of the dished shape and do not exist for flat grids.

The third thrust loss is due to the divergence of the ion trajectories comprising each beamlet. This loss probably depends upon the aperature geometry, ion sheath shape, and the applied potentials. Theoretical beamlet divergence studies have been investigated in references 9 and 10.

The thrust loss associated with the angle λ can be eliminated if the dished grid geometry can be made with its aperatures co-axial as shown in figure 3c. Further reduction of the γ thrust loss can be achieved by properly misalining the aperatures so that negative λ values are obtained. Thus, for $\lambda = -\gamma$ as shown in figure 3d the resultant ion beamlet vectors are axially directed and only beamlet divergence losses are incurred.

The thrust losses will be discussed from the three general sources in the following order: (1) hole misalinement, (2) grid curvature, and (3) losses due to ion curvatures in individual beamlets. To assess the effects of hole misalinement the thrust losses as a function of grid compensation, percent open area, and grid spacing on thrust losses are presented. The effects of dish depth on thrust losses are discussed next. Lastly, the effects of parameters which change the trajectories in each individual beamlet are discussed. These include hole size, total ion beam current, total accelerating voltage, and the ratio of net-to-total accelerating voltage. For the sake of completeness all of the data taken are presented in table II. The data is separated into two sections corresponding to the two probe positions. As mentioned earlier, a number of different thrusters were run during the course of this study. Since the thrust factor was not sensitive to thruster variation this information is not included in the table.

Hole Misalinement

By far the largest improvement in thrust factor was accomplished by the use of dished grid sets where the accelerator grid was compensated to minimize thrust losses. Figure 4 shows the thrust factor as a function of strain of the accelerator grid (grid sets B1, C1, D1, and E1). This effect can also be seen dramatically in figure 5 which presents computer generated contour plots from the

probe rake data for grids for which the strain of the accelerator grid, ε, was 0.0000, 0.0022, and 0.0066, respectively. The contour plots show very effectively how the compensated grids narrow the spread in the thruster beam. It is interesting to note from figure 4 that the best experimental strain for the accelerator grid appears to be larger than the value predicted by the expression for $\varepsilon_{\lambda=-\gamma}$ given in appendix B. Using the parameters for grid sets B1, C1, D1, and E1 from table I gives $\varepsilon_{\lambda=-\gamma} = 0.0045$. Note that one limit on the best experimental strain would be when direct ion impingement begins to occur. This occurs only for grid set K1 in this study.

The percent open area of the grids was also varied. Data from grid set B1 (51 percent open area) can be compared with data from grid set F2 (67 percent open area). Both are uncompensated grid sets. Data run numbers 65, 68, and 69 when compared with runs 81, 85, and 86, respectively, show that the increase in open area from 51 to 67 percent caused approximately a 0.6 percent decrease in thrust factor. It is possible that for the higher open area grids that the sheaths from neighboring grid holes overlap in such a way as to amplify the effects of misalinement. This point is discussed in more detail in a companion paper (ref. 5).

The cold grid gap was varied on a number of grid sets. The effect on the thrust factor was quite small. Small variations in the cold gap actually led to data that sometimes increased and sometimes decreased the thrust factor. For grid set P where the gap was decreased by more than a factor of two the thrust factor increased by only 0.4 percent.

Grid Curvature

Data were taken with two hexagonal hole grid sets (grid sets O and P) with different dish depths. Grid set O with the shallower dish also had an accelerator grid that was slightly compensated ($\varepsilon = 0.00097$) making quantitative comparisons difficult. Grid set O did lead to less thrust loss. However, how much of the improvement came from the shallower dish shape and how much from the compensation of the accelerator grid can not be determined.

Individual Beamlet Losses

The remaining parameters primarily affect the distribution of ions within the individual beamlets from each set of holes. Run numbers 81, 85, and 86 (grid set B1) when compared with run numbers 100 to 102 (grid set A1), respectively, show the effect of hole size on the thrust factor. An increase in hole diameter from 0.102 to 0.178 centimeter corresponded to approximately a 0.5 percent gain in the thrust factor. Comparisons of runs 20 (grid set G1) against 42 (grid set F1) and 113 (grid set M2) against 129 (grid set H1) further show thrust factor gains of 0.8 and 0.3 percent, respectively, with an increase in hole diameter. This is probably due to the spreading out of the ion trajectories in the individual beamlets for the smaller holes.

Figure 6 shows the effect of total ion beam current J_B on the thrust factor with both compensated and uncompensated grids. These data were taken for almost every grid set. Typically, there was no change in thrust factor with total ion beam current for uncompensated grids. On the other hand with the compensated grid sets there was an increase in thrust factor with total ion beam current.

It has not been determined why these differences occur. Close beam traces within a few centimeters of the thruster showed no change in normalized beam profile with total ion current for any of the grids studied. Also, the deliberate misalinement of the compensated grids is always much larger than the original slight misalinement of the uncompensated grids. It is possible that a fixed amount of compensation leads to varying amounts of deflection with increased beam current. This could account for the differences in thrust factor with beam current for the uncompensated and compensated grid sets.

Figure 7 shows the effect of R ratio (screen voltage V_I divided by total voltage $V_I + |V_A|$) on the thrust factor. The data were taken three ways: with V_I constant (grid sets L1 and H1), with V_A constant (grid set H1), and with $V_I + |V_A|$ constant (grid set L1). It can be seen from the data in table II that higher R ratios led to higher thrust factors regardless of which way the data were taken. This indicates that total voltage is not important, only the R ratio is. Therefore, thrust losses can be reduced by operating a thruster at as high an R ratio as possible without backstreaming.

Error Analysis

In the discussions of the data above it is desirable to have some indication of the repeatability of the data. Twenty-nine runs in the table are repeated. Sometimes points were repeated when it was not certain that the data had been received properly by the CADDE system. In addition some earlier runs (grid set F1, runs 34-41) were made with some variations which it was felt would not affect the thrust factor. Varied in these runs were probe speed, position on the ev/ion-utilization curve, neutralizer flow rate, and the differences with other nearby facilities being on or off. For these eight runs the thrust factor was either 0.905 or 0.906 indicating that the data were quite repeatable. The only repeated data which were different by more than 0.2 percent were points 169 and 170 which differed by 0.3 percent and points 148 and 150 which differed by 0.4 percent.

As mentioned in the section on the computer code it is assumed in calculating the thrust factor that all of the current comes from a point source at the center of the grids. This approximation leads to overestimates in the calculated thrust losses. This is because current from the outer portions of the grids to a particular probe position will arrive more nearly perpendicular to the probe than assumed for the point source approximation. The farther the probe rake is from the grids the better the point source approximation becomes. The data up to run number 182 were taken with the probe rake 1.37 meters downstream of the grids. The data for run numbers 183 and higher were taken with the probe rake 1.83 meters downstream of the grids. Because of the point source approximation improving with the increase in this distance, the later data

leads to thrust factors approximately 1 percent higher than the earlier data. At this distance the point source approximation is still undercalculating the thrust factor by some unknown amount.

The molybdenum probes were biased negatively to repel thermal electrons. As part of this study the effects of secondary electron emission on the data using a Faraday cup indicated that this had less than a 0.5 percent effect on the current densities measured. Another indication that the measured current densities were accurate was that calculated values of total ion current were almost always within 2 percent of the meter value. The effect on the thrust factor would be a very small fraction of a percent since the current densities appear in both the numerator and denominator of the expression for T.

Computer errors due to curve fitting the data and the integration techniques used are estimated to be less than 0.2 percent. The effects of double ionization on the thrust factor have been ignored in this study and are unknown at this time.

Conclusions

A procedure has been developed for accurately measuring beam divergence from 30-centimeter diameter dished grids. Techniques have also been developed for stretching the accelerator grid of a grid set to compensate for thrust losses inherent in a dished grid system. Through the variation of a number of parameters it was possible to reduce the thrust losses from beam divergence to less than 2 percent. Further reductions in thrust loss will probably be small since some beam divergence will always be present due to the ion trajectories in individual beamlets not being perfectly parallel.

Appendix A

Symbol List

g	grid gap, m
h	dish depth, m
j	current density, amp/m^2
J_B	total ion beam current, amp
k	constant of proportionality, dimensionless
ℓ	arc length from grid center to outermost active grid hole, m
R	ratio of net to total accelerating voltage, dimensionless
R	radius of curvature of dished grid, m
r	radius as defined in equations (1) and (2), m
r_D	radius of the dished portion of the grid, m
r_H	radius of the outermost active region of the dished grid, m
T	thrust factor, dimensionless
t_A	accelerator grid thickness, m
t_s	screen grid thickness, m
V_I	screen voltage, volts
V_A	accelerating voltage, volts
γ	angle between the thruster axis and a line perpendicular to the grid surface at the outermost active hole, radians
$\Delta\ell$	change in ℓ due to stretching grid, m
δ	misalinement of the outermost holes required to produce para-axial beamlets, m
ε	strain, dimensionless
$\varepsilon_{\lambda=0}$	strain required to produce co-axial screen and accelerator grid holes, dimensionless
$\varepsilon_{\lambda=-\gamma}$	strain required to produce para-axial ion beamlets, dimensionless
ψ	angle defined in equations (1) and (2), radians
θ	angle defined in equations (1) and (2), radians

Appendix B

Strain Compensation Required For Reduction Of Dished Grid Thrust Losses

The required strain of the accelerator grid, $\varepsilon_{\lambda=0}$, to compensate for the λ thrust loss for outermost holes is a function of grid gap g, screen grid thickness t_s, accelerator grid thickness t_A, dished grid radius of curvature R, and the angle γ between the thruster axis and a line perpendicular to the grid surface at the outermost active hole. Relating these variables through the use of figure 3 one obtains

$$\varepsilon_{\lambda=0} = \frac{\Delta\ell}{\ell} \tag{B1}$$

or

$$\varepsilon_{\lambda} = \frac{g + \left(\frac{t_s + t_A}{2\cos\gamma}\right)\sin\gamma}{R\gamma} \tag{B2}$$

but

$$R^2 = r_D^2 + (R - h)^2 \tag{B3}$$

so that

$$R = \frac{r_D^2 + h^2}{2h} \tag{B4}$$

and

$$\sin\gamma = \frac{2r_H h}{r_D^2 + h^2} \tag{B5}$$

Using these relations an expression for $\varepsilon_{\lambda=0}$ can be obtained.

$$\varepsilon_{\lambda=0} = \frac{2r_H h^2 \left(\frac{2g}{r_D^2 + h^2} + \frac{t_s + t_A}{r_D^2 - h^2} \right)}{\left(r_D^2 + h^2 \right) \arcsin \left(\frac{2r_H h}{r_D^2 + h^2} \right)} \quad \text{(B6)}$$

This represents a geometry in which the outermost holes are in the proper position to have coaxial hole centerlines. For example if $g = 0.0635$ centimeter (0.025 in.), $t_s = 0.0381$ centimeter (0.015 in.), $t_A = 0.0762$ (0.030 in.), $h = 2.286$ centimeter (0.9 in.), $2r_H = 28.448$ centimeters (11.2 in.) and $2r_D = 30.480$ centimeters (12.0 in.) then $\varepsilon_{\lambda=0} = 0.00234$.

Compensation to produce para-axial beamlets requires additional stretching and the total strain is given by

$$\varepsilon_{\lambda=-\gamma} = \varepsilon_{\lambda=0} + \frac{\delta}{R\gamma} \quad \text{(B7)}$$

where δ is the misalinement of the outermost holes to produce para-axial beamlets. Lathem and Adam have shown in references 9 and 10 for a given grid geometry, spacing, and beam current deflection, that γ is approximately proportional to the grid translation fraction δ/d_A, where d_A is the accelerator hole diameter.

Thus, if k is the constant of proportionality then

$$\gamma = k \frac{\delta}{d_A} \quad \text{(B8)}$$

or

$$\delta = \frac{\gamma d_A}{k} \quad \text{(B9)}$$

and

$$\varepsilon_{\lambda=-\gamma} = \varepsilon_{\lambda=0} + \frac{\gamma d_A}{Rk\gamma} \quad \text{(B10)}$$

or

$$\varepsilon_{\lambda=-\gamma} = \varepsilon_{\lambda=0} + \frac{d_A}{Rk} \quad \text{(B11)}$$

and

$$\varepsilon_{\lambda=-\gamma} = \frac{2r_H h^2 \left(\frac{2g}{r_D^2 + h^2} + \frac{t_s + t_A}{r_D^2 - h^2} \right)}{\left(r_D^2 + h^2 \right) \arcsin \left(\frac{2r_H h}{r_D^2 + h^2} \right)} + \frac{2hd_A}{\left(r_D^2 + h^2 \right) k} \quad \text{(B12)}$$

Values of k in reference 10 vary from 1.84 to 1.33 depending upon the grid system geometry, grid gap, and ion beam current. The first and second term of the $\varepsilon_{\lambda=-\gamma}$ equation are of near equal magnitude. It can also be shown that this value of strain is within 1/2 percent of the ideal strain value for the entire grid face even though the calculation was made for the outermost active holes.

Table I Dished Grid Geometries

Grid set	Hole Diam, mm		Grid Thickness, mm		Open Area Fraction		Strain	Dish Depth to Dish Diam Ratio	Hole Shape	Cold Grid To Grid Spacing, mm	Run Nos. Table II
	Screen	Accel	Screen	Accel	Screen	Accel	%				
A1	1.02	1.02	0.38	0.38	0.51	0.51	0	0.075	Circular	0.64	100-106
B1	1.91	1.91	0.38	0.38	0.51	0.51	0	0.075	Circular	0.64	81-86
B2	↓	↓	↓	↓	↓	↓	↓	↓	↓	0.66	48-63
B3	↓	↓	↓	↓	↓	↓	↓	↓	↓	0.99	45-47
C1	1.91	1.91	0.38	0.38	0.51	0.51	0.22	0.075	Circular	0.64	71-80
D1	1.91	1.91	0.38	0.38	0.51	0.51	0.44	0.075	Circular	0.86	218-239
E1	1.91	1.91	0.38	0.38	0.51	0.51	0.66	0.075	Circular	0.76	188-195
E2	↓	↓	↓	↓	↓	↓	↓	↓	↓	0.84	144-166
E3	↓	↓	↓	↓	↓	↓	↓	↓	↓	1.09	93-99
F1	1.91	1.91	0.38	0.38	0.67	0.67	0	0.075	Circular	0.74	28-43
F2	1.91	1.91	0.38	0.38	0.67	0.67	0	0.075	Circular	0.76	65-69, 143,167, 196-201
G1	2.41	2.41	0.38	0.38	0.67	0.67	0	0.075	Circular	0.64	20,107
G2	2.41	2.41	0.38	0.38	0.67	0.67	0	0.075	Circular	1.14	22
H1	1.91	1.52	0.38	0.76	0.67	0.43	0	0.075	Circular	0.69	128-142
H2	↓	↓	↓	↓	↓	↓	↓	↓	↓	0.84	202,214
H3	↓	↓	↓	↓	↓	↓	↓	↓	↓	1.30	87-88
J1	1.91	1.52	0.38	0.76	0.67	0.43	0.35	0.075	Circular	0.81	207-213
K1	1.91	1.52	0.38	0.76	0.67	0.43	1.3	0.075	Circular	0.51	215,217
L1	2.16	1.73	0.38	0.76	0.67	0.43	0	0.075	Circular	1.02	115-127
M1	2.41	1.93	0.38	0.76	0.67	0.43	0	0.075	Circular	0.94	114
M2	2.41	1.93	0.38	0.76	0.67	0.43	0	0.075	Circular	1.24	108-113
N1	2.41	1.93	0.38	0.76	0.67	0.43	0.25	0.038	Circular	0.89	240-244
O1	2.08	2.08	0.38	0.38	0.77	0.77	0	0.075	Hexagonal	0.91	90
O2	2.08	2.08	0.38	0.38	0.77	0.77	0	0.075	Hexagonal	1.14	91,92
P1	2.08	2.08	0.38	0.38	0.77	0.77	0.097	0.038	Hexagonal	0.91	177-187
P2	↓	↓	↓	↓	↓	↓	↓	↓	↓	1.17	173-176
P3	↓	↓	↓	↓	↓	↓	↓	↓	↓	1.98	168-172

Table II Thrust Factor Data

Probe Position 1					
Grid Set	Data Run Number	Net Ion Accelerating Voltage, volts	Accelerator Grid Voltage, volts	Beam Current, amps	Thrust Factor
A1	100	1100	500	1.00	0.914
	101	↓	500	1.51	.911
	102		500	2.00	.911
	103		150	↓	.925
	104		300		.918
	105		500		.911
	106		750	2.00	.905
B1	81	1100	500	2.00	0.919
	82	↓	450	↓	.921
	83		750		.912
	84		500		.917
	85		500	1.50	.919
	86	1100	500	1.00	.918
B2	48	800	400	1.00	0.910
	49	1000	500	1.50	.908
	62	800	400	1.00	.912
	63	1000	500	2.03	.913
B3	45	800	400	1.00	0.911
	46	1000	500	1.50	.912
	47	1200	600	2.00	.910
C1	71	1100	500	2.00	0.956
	72	700	300	↓	.943
	73	1200	400		.954
	74	1100	500		.955
	75	1000	500		.953
	76	1100	400		.956
	77	1100	750		.950
	78	1100	1100	2.00	.938
	79	1100	500	1.50	.951
	80	1100	500	1.00	.946
E2	144	1100	500	2.00	0.966
	145	1400	650	↓	.965
	148	1300	600		.965
	149	1200	550		.966
	150	1300	600		.969
	153	1200	400		.968
	154	1100	500		.965
E2	155	1100	500	2.00	0.966
	156	1000	600	↓	.965
	157	900	700		.962
	158	800	800		.960
	159	700	900		.956
	160	600	1000		.953
	161	500	1100		.947
	164	400	1200		.937
	165	1100	500	1.50	.964
	166	1100	500	1.00	.956
E3	93	1100	500	1.00	0.961
	94	↓	↓	1.50	.970
	96			2.00	.974
	97			2.00	.974
	98		750	2.00	.967
	99		1100	2.00	.955
F1	28	1000	500	2.00	0.906
	29	750	750	↓	.890
	30	500	1000		.870
	31	750	750		.890
	32	1500	500		.914
	33	1000	↓	↓	.906
	34	↓			↓
	35				
	36				
	37				
	38				
	39				.905
	40				.905

Table II Continued

Grid Set	Data Run Number	Net Ion Accelerating Voltage, volts	Accelerator Grid Voltage, volts	Beam Current, amps	Thrust Factor
F1	41	1000	500	2.00	0.906
	42	1200	600	2.50	.906
	43	1200	600	2.50	.907
F2	65	1100	500	2.00	0.913
	66	1300	↓	2.00	.914
	67	1100	↓	2.00	.914
	68	1100	↓	1.50	.915
	69	↓	↓	1.00	.912
	143	↓	↓	1.99	.912
	167	↓	↓	2.01	.908
G1	20	1200	600	2.50	0.914
G2	22	1460	870	3.00	0.910
H1	128	1100	500	1.99	0.909
	129	1100	↓	2.01	.911
	131	700	↓	2.00	.902
	132	900	↓	↓	.908
	133	1100	↓	↓	.912
	135	1200	↓	↓	.912
	136	1300	↓	↓	.912
	137	1400	↓	↓	.912
	138	1500	↓	↓	.913
	139	1100	300	↓	.918
	140	1100	400	↓	.916
	141	1100	600	↓	.906
	142	1100	800	↓	.897
H3	87	1100	500	1.01	0.903
	88	1100	500	1.49	.902
L1	115	1100	500	1.00	0.915
	117	↓	300	2.00	.921
	118	↓	500	↓	.915
	119	↓	800	↓	.907
	121	↓	1100	↓	.901
	122	800	800	↓	.901
	123	950	650	↓	.909
	124	1100	500	↓	.916
	125	1300	300	↓	.924
	126	1100	500	1.50	.917
	127	1100	500	1.00	.914
M1	114	1100	500	1.52	0.918
M2	108	1100	500	1.00	0.918
	109	1200	700	1.50	.914
	110	1100	500	1.50	.917
	111	1400	700	2.00	.916
	112	1300	650	2.00	.915
	113	1100	500	2.00	.914
	114	1100	500	1.52	.918
O1	90	500	420	1.00	0.937
O2	91	1100	500	1.00	0.937
	92	1100	500	2.00	.940
P1	177	1100	500	1.00	0.950
	178	↓	↓	1.50	.962
	180	↓	↓	2.00	.965
	182	↓	↓	2.00	.965
P2	173	1100	500	1.00	0.957
	174	1100	500	1.50	.960
	175	1100	500	2.00	.960
	176	1300	600	2.00	.960
P3	168	1100	500	1.00	0.957
	169	↓	↓	1.50	.959
	170	↓	↓	1.51	.956
	171	↓	600	2.00	.959
	172	1100	600	2.00	.960

Table II Concluded

Probe Position 2					
Grid Set	Data Run Number	Net Ion Accelerating Voltage, volts	Accelerator Grid Voltage, volts	Beam Current, amps	Thrust Factor
D1	219	1250	350	2.00	0.977
	220	1100	500	↓	.974
	221	900	700	↓	.970
	222	700	900	↓	.965
	223	500	1100	↓	.954
	224	1100	500	1.50	.971
	225	1080	520	1.51	.971
	226	800	400	1.50	.971
	227	1000	500	↓	.971
	228	1250	350	↓	.974
	229	1000	600	↓	.970
	230	700	900	↓	.962
	233	400	1200	↓	.942
	234	1250	350	1.00	.966
	235	1100	500	↓	.964
	236	800	800	↓	.957
	237	400	1200	↓	.935
	238	1100	500	.50	.952
	239	1100	500	.50	.950
E1	188	1100	500	1.00	0.966
	189	1100	500	1.50	.974
	190	1100	500	2.01	.979
	191	1250	350	2.02	.981
	192	900	700	2.00	.973
	193	600	1000	↓	.959
	194	1100	350	↓	.980
	195	1100	700	↓	.974
F2	196	1100	500	2.00	0.924
	199	1100	500	1.81	.925
	201	1100	500	2.00	.922
H2	202	1100	500	2.00	0.924
	214	1075	500	1.92	.924
J1	207	1075	500	1.92	0.951
	208	1075	500	1.91	.952
	209	1075	500	1.97	.956
	210	1200	400	1.32	.957
	213	1075	500	.97	.947
K1	217	1100	300	0.13	0.960
N1	240	1100	500	2.00	0.977
	241	1080	400	1.93	.979
	242	1200	400	1.31	.976
	243	1200	400	1.34	.965
	244	1320	360	.81	.968
P1	183	1100	500	1.01	0.963
	184	600	400	1.00	.963
	185	1100	500	1.51	.967
	186	1100	600	2.01	.967
	187	1100	500	2.01	.969

REFERENCES

1. Bartz, D. R., and Horsewood, J. L., "Characteristics, Capabilities, and Costs of Solar Electric Spacecraft for Planetary Missions," Journal of Spacecraft and Rockets, Vol. 7, No. 12, Dec. 1970, pp. 1379-1390.

2. Strack, W. C., and Hrach, F. J., "Early Application of Solar-Electric Propulsion of a 1-Astronomical-Unit Out-of-the-Ecliptic Mission," TN D-5996, 1970, NASA, Cleveland, Ohio.

3. Rawlin, V. K., Banks, B. A., and Byers, D. C., "Design, Fabrication, and Operation of Dished Accelerator Grids on a 30-cm Ion Thruster," Paper 72-486, Apr. 1972, AIAA, New York, N.Y.

4. King, H. J., and Poeschel, R. L., "Low Voltage 30 cm Ion Thruster," NASA CR-120919, Feb. 1972, Hughes Research Labs., Malibu, Calif.

5. Rawlin, V. K., "Performance of 30-cm Ion Thrusters with Dished Accelerator Grids," to be published.

6. Finke, R. C., Holmes, A. D., and Keller, T. A., "Space Environment Facility for Electric Propulsion Systems Research," TN D-2774, 1965, NASA, Cleveland, Ohio.

7. Staff of Lewis Research Center, "Central Automatic Data Processing System," TN-4212, 1958, NACA, Cleveland, Ohio.

8. Akima, H., "A New Method of Interpolation and Smooth Curve Fitting Based on Local Procedures," Journal of the Association for Computing Machinery, Vol. 17, No. 4, Oct. 1970, pp. 589-602.

9. Lathem, W. C., "Approximate Analysis of the Effects of Electrode Misalinements on Thrust Vector Control in Kaufman Thrusters," Paper 68-89, Jan. 1968, AIAA, New York, N.Y.

10. Lathem, W. C., and Adam, W. B., "Theoretical Analysis of a Grid-Translation Beam Deflection System for a 30-cm Diameter Kaufman Thruster," TM X-67911, 1971, NASA, Cleveland, Ohio.

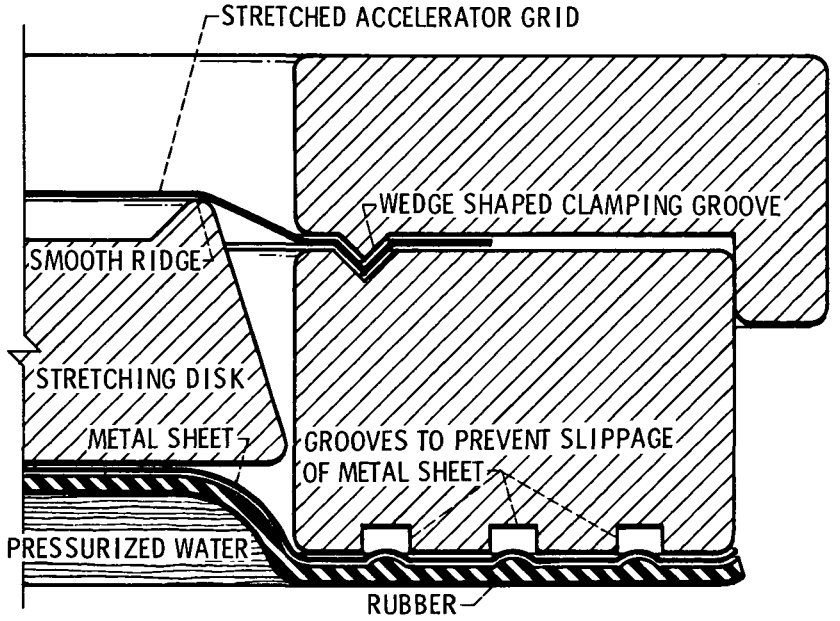

Figure 1. - Stretching system for accelerator grid.

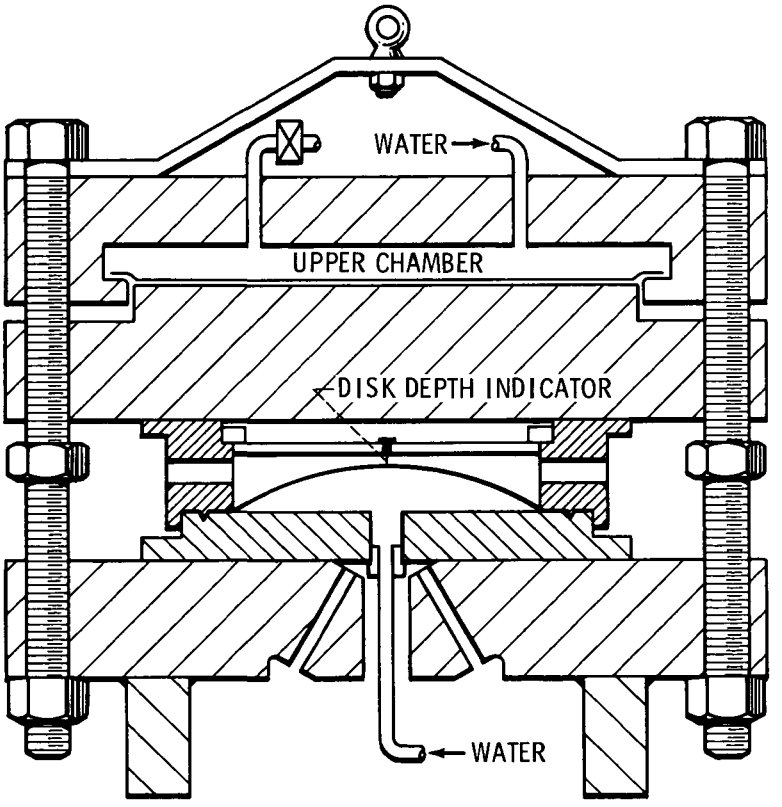

Figure 2. - Section view of hydroforming system.

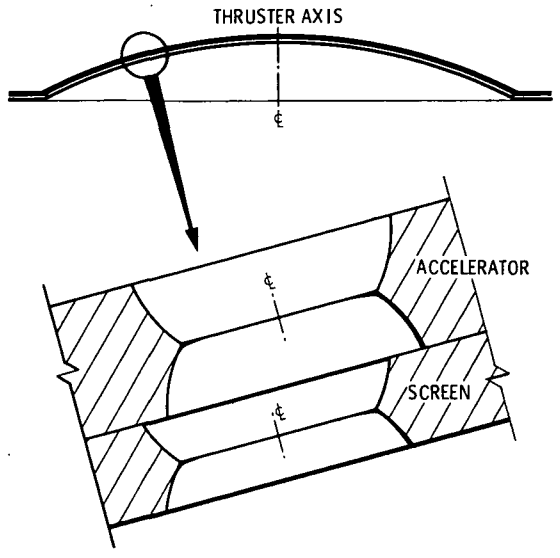

(a) AFTER SIMULTANEOUSLY HYDROFORMING THE CENTERS OF THE GRID HOLES ARE LOCATED APPROXIMATELY DOWNSTREAM OF EACH OTHER (NO COMPENSATION).

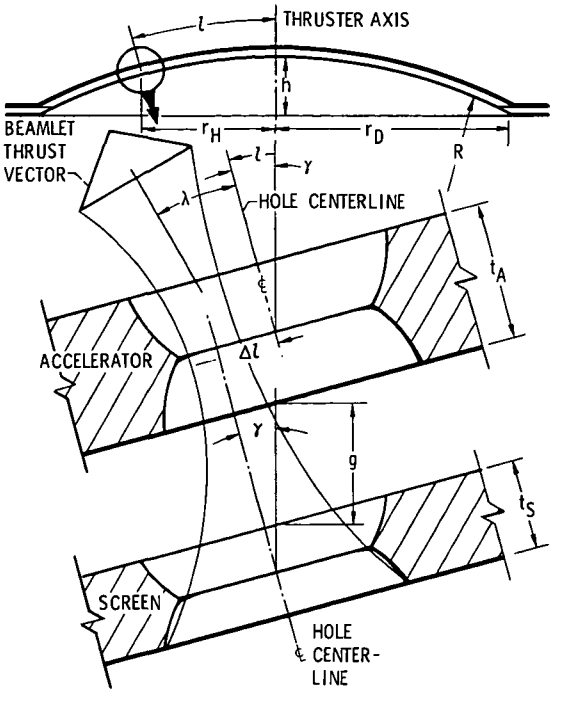

(b) AXIALLY DISPLACED DISHED GRIDS (NO COMPENSATION).

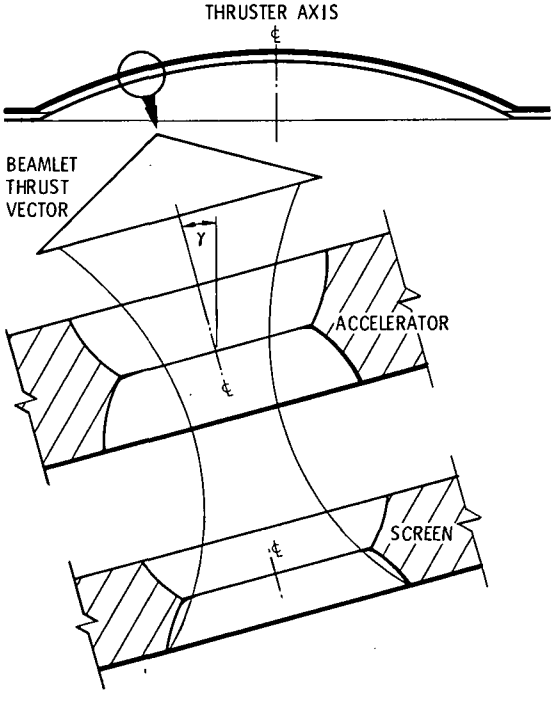

(c) DISHED GRIDS WITH COAXIAL APERATURES WHICH ELIMINATE THE λ THRUST LOSS.

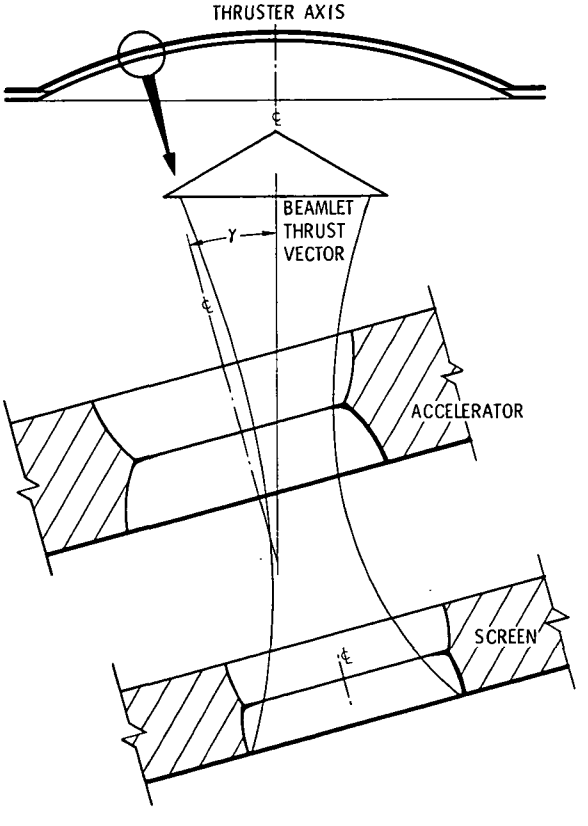

(d) DISHED GRID COMPENSATED FOR λ AND γ THRUST LOSSES.

Figure 3. - Section views of dished grid configurations.

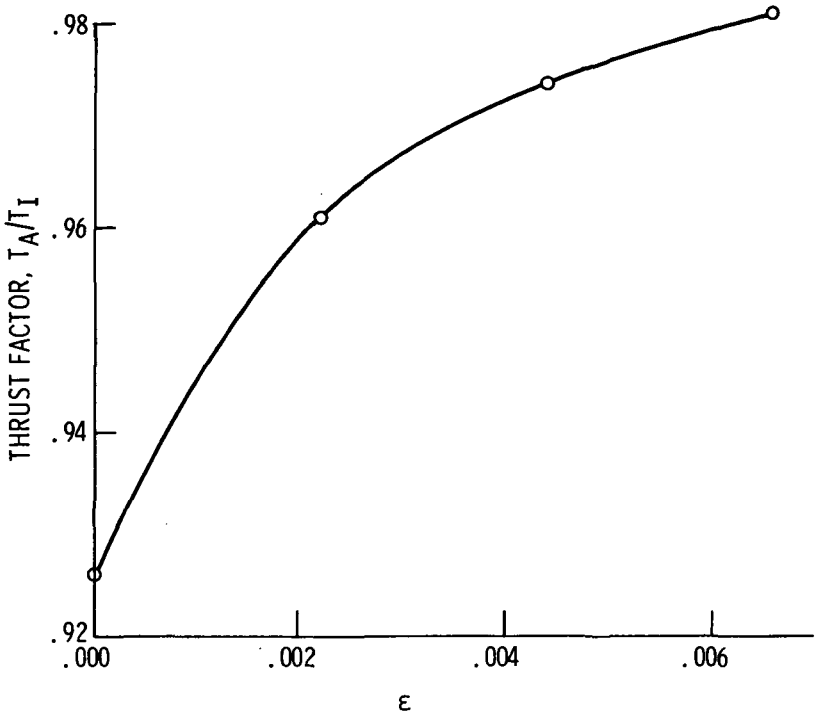

Figure 4. - Thrust factor versus strain of accelerator grid.

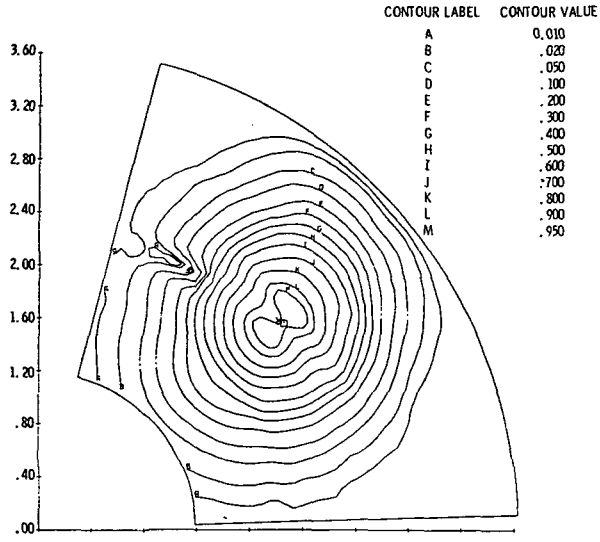

(a) CONTROU PLOT FOR AN UNCOMPENSATED GRID SET (ε = 0.0000).

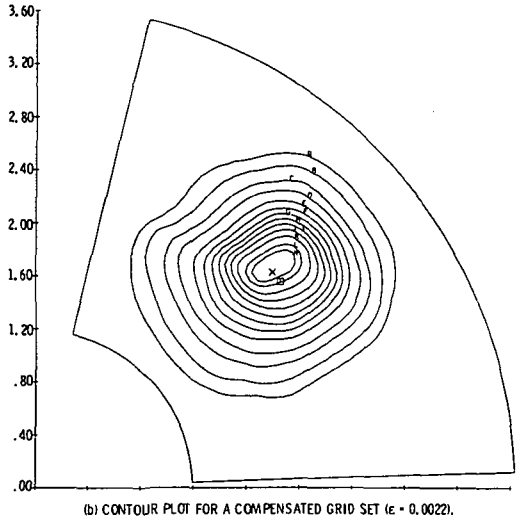

(b) CONTOUR PLOT FOR A COMPENSATED GRID SET (ε = 0.0022).

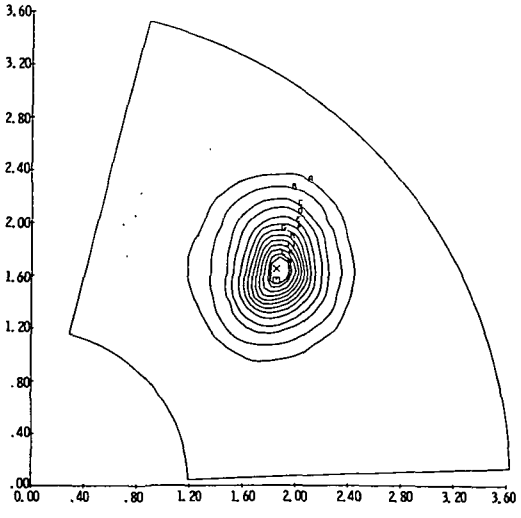

(c) CONTOUR PLOT FOR A COMPENSATED GRID SET (ε = 0.0066).

Figure 5. - Beam contour plots.

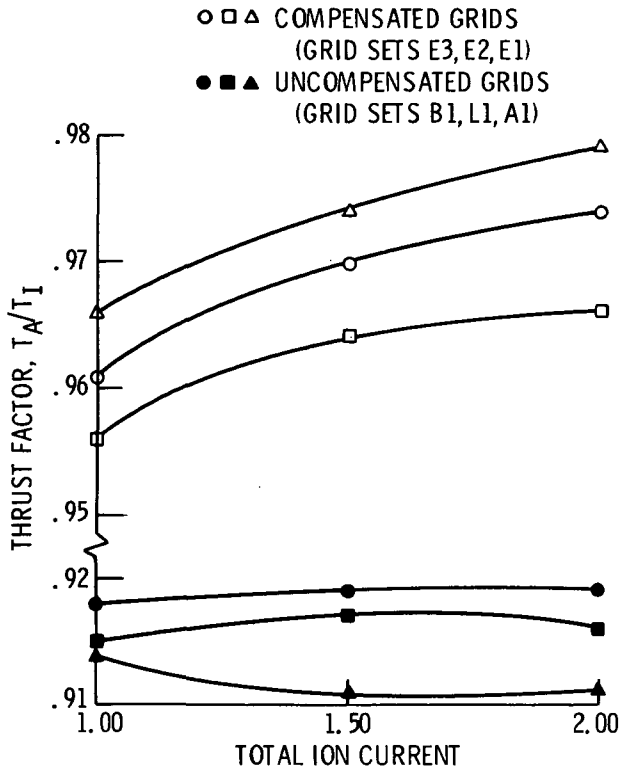

Figure 6. - Thrust factor versus total ion current.

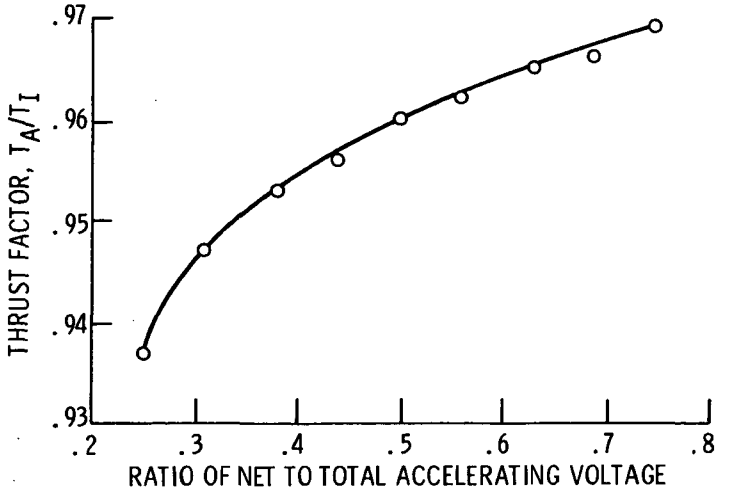

Figure 7. - Thrust factor versus ratio of net to total accelerating voltage for grid set E2.